SCIENTIFIC REPORTS

OPEN

Metamaterial Perfect Absorber Analyzed by a Meta-cavity Model Consisting of Multilayer Metasurfaces

Received: 28 April 2017
Accepted: 9 August 2017
Published online: 05 September 2017

Khagendra Bhattarai[1], Sinhara Silva[1], Kun Song[2], Augustine Urbas[3], Sang Jun Lee[4], Zahyun Ku[3] & Jiangfeng Zhou[1]

We demonstrate that the metamaterial perfect absorber behaves as a meta-cavity bounded between a resonant metasurface and a metallic thin-film reflector. The perfect absorption is achieved by the Fabry-Perot cavity resonance via multiple reflections between the "quasi-open" boundary of resonator and the "close" boundary of reflector. The characteristic features including angle independence, ultra-thin thickness and strong field localization can be well explained by this meta-cavity model. With this model, metamaterial perfect absorber can be redefined as a meta-cavity exhibiting high Q-factor, strong field enhancement and extremely high photonic density of states, thereby promising novel applications for high performance sensor, infrared photodetector and cavity quantum electrodynamics devices.

The metamaterial perfect absorber (MPA), exhibiting nearly unity absorption within a narrow frequency range[1–6], has attracted tremendous interest recently. The MPA possesses characteristic features of angular-independence, high *Q*-factor and strong field localization that have inspired a wide range of applications including electromagnetic (EM) wave absorption[3,7,8], spectral[5] and spatial[6] modulation of light, selective thermal emission[9], thermal detection[10], infrared photo detection[11–14], circularly polarized light detection[15–17], and refractive index sensing for gas[18] and liquid[19–21] targets. The MPA typically consists of three layers: an array of metallic resonators (e.g., cross-type resonators[9,22], split-ring resonators[3] or metallic nanoparticles[23] and chiral resonators[15,24]) and a highly reflective layer (e.g. metallic film[3,9,22,23] or metallic mesh grid[3]), separated by a subwavelength-thick dielectric film (spacer). The mechanism of MPA has been explained through a number of models including impedance matching[3,7,25] and destructive interference[26]. In the impedance matching mechanism, the entire three-layered structure is considered as a thin slab made from a homogeneous medium with frequency-dependent effective permittivity $\in_{\text{eff}}(\omega)$ and effective permeability $\mu_{\text{eff}}(\omega)$. At the perfect absorbing frequency (ω_0), the effective permittivity and permeability reach the same value ($\epsilon_{\text{eff}}(\omega)|_{\omega=\omega_0} = \mu_{\text{eff}}(\omega)|_{\omega=\omega_0}$), so that the impedance (both real and imaginary parts) matches to the free space, $z_{\text{eff}}(\omega)|_{\omega=\omega_0} = z_{\text{eff}}{}'(\omega_0) + iz_{\text{eff}}{}''(\omega_0) = 1$. Meanwhile, the effective refractive index $n_{\text{eff}}(\omega)$ at $\omega = \omega_0$ exhibits a large imaginary part, $n_{\text{eff}}{}''(\omega_0) \gg n_{\text{eff}}{}'(\omega_0)$, thus incident EM wave enters MPA without any reflection and then rapidly decays to zero inside the MPA. In the destructive interference mechanism, the resonator and the metallic film are considered as two decoupled surfaces, and destructive interferences of waves reflected multiple times by two surfaces lead to zero reflection[26,27].

In this work, we use a transfer matrix method to assemble the MPA from three functional layers and obtain the phase and the amplitude conditions for the perfect absorption. Analyzing these conditions, we reinterpret the MPA structure as a meta-cavity bounded between a "quasi-open" boundary of a resonant metasurface and a "close" boundary of a metallic film. The Fabry-Perot (FP) modes are achieved when the phase condition is satisfied, which leads to a strong resonance with non-perfect absorption (NPA). However, the perfect absorption (PA) only occurs when both the phase and the amplitude conditions are satisfied simultaneously. Although PA

[1]Department of Physics, University of South Florida, Tampa, 33620, USA. [2]Smart Materials Laboratory, Department of Applied Physics, Northwestern Polytechnical University, Xi'an, 710129, China. [3]Materials and Manufacturing Directorate, Air Force Research Laboratory, 45433, Wright-Patterson AFB, USA. [4]Division of Convergence Technology, Korea Research Institute of Standards and Science, Daejeon, 34113, Korea. Khagendra Bhattarai, Sinhara Silva and Kun Song contributed equally to this work. Correspondence and requests for materials should be addressed to S.J.L. (email: sjlee@kriss.re.kr) or Z.K. (email: zahyun.ku.1.ctr@us.af.mil) or J.Z. (email: jiangfengz@usf.edu)

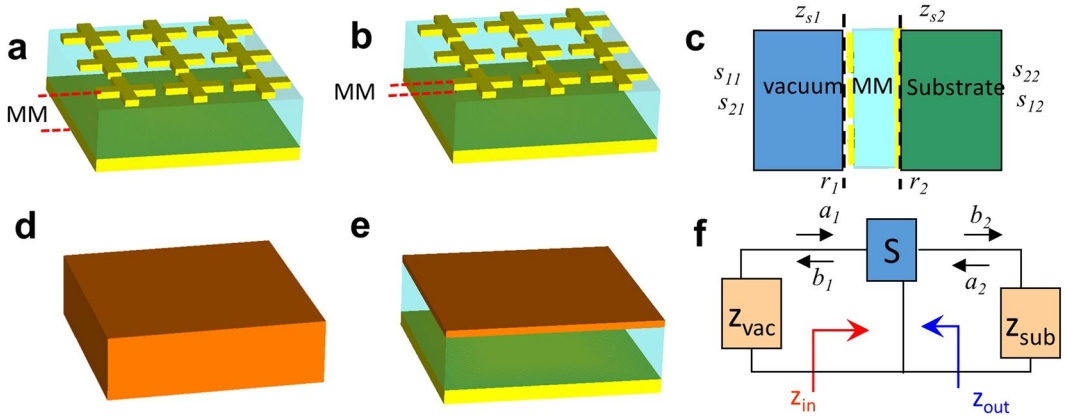

Figure 1. Effective models for MPA. Schematic diagrams of (**a**) metamaterial perfect absorber (MPA) and its (**d**) equivalent single-layer film characterized by effective ϵ_{eff} and μ_{eff}; (**b**) perfect absorber with cross-wire, spacer and metal ground plate considered as a three-layer structure and (**e**) equivalent three-layer film model where the cross-wire is considered by a homogeneous film with ϵ_{eff} and μ_{eff}. (**c**) View of perfect absorber along wave propagation direction. The MPA is surrounded by air and a dielectric substrate with optical impedances z_{s1} and z_{s2} at two interfaces, respectively. (**f**) A transmission line model uses a two-port network S to describe the MPA, where z_1 and z_2 are impedances of air and substrate, and z_{in} and z_{out} are input and output impedances of S, respectively.

has drawn significant attention, NPA are more commonly used in practical applications such as sensors[18–21,28] and detectors[10–14]. Both PA and NPA can be well explained by the meta-cavity model. With an improved retrieval method, we find that the resonant metasurface operates at off-resonance wavelengths, thereby acting as a homogenous thin film with high dielectric constant. The FP model redefines MPA as a meta-cavity with high Q-factor and extremely high photonic density of states (PDOS) where the FP modes are easily tailored by the geometric parameters of metasurface. Our work can pave the way for novel photonic, optoelectronic and cavity quantum electrodynamic (QED) applications[29].

Results

Single-layer effective medium model. Our perfect absorber consists of three layers: an array of cross-wire resonators, a dielectric spacer and a metal ground plane (MGP) as shown in Fig. 1a. We carry out a 3D full-wave simulation to solve Maxwell's equations and obtain numerical solutions by Computer Simulation Technology Microwave Studio that uses a finite integration technology[30]. The parameters used for simulation are as follows: period of cross-wire array, $p = 2\ \mu m$, length and width of the cross-wire, $l = 1.7\ \mu m$ and $w = 0.4\ \mu m$, permittivity of GaAs substrate and a dielectric spacer, $\varepsilon_{GaAs} = 11.56$ and $\varepsilon_s = 2.28$, thickness of the dielectric spacer, $t_s = 0.09\ \mu m$, and thickness of cross-wire and MGP, $t_{c-w} = t_{MGP} = 0.1\ \mu m$. The gold used for cross-wire and MGP is described by the Drude model[31] with plasma frequency, $\omega_p = 1.37 \times 10^{16}\ rad/s$ and collision frequency $\omega_c = 4.08 \times 10^{13}\ rad/s$. We use three different models to describe the perfect absorber: (i) A single-layer effective medium model where the entire structure (Fig. 1a) is considered as a layer of homogeneous medium (Fig. 1d) characterized by the effective permittivity (ϵ_{eff}) and effective permeability (μ_{eff}); (ii) A three-layer effective medium model where the cross-wire resonator (Fig. 1b) is considered as a homogeneous effective film (Fig. 1e) with ϵ_{eff} and μ_{eff} on top of two layers of real films, the spacer and MGP; (iii) A transmission line model where the multiple-layer optical system (Fig. 1c) is modeled as a two-port network (Fig. 1f) with input impedance z_{in} and output impedance z_{out}.

Since the MGP prevents the EM wave from propagating through, the perfect absorption is obtained when the reflection reaches zero at certain wavelength as shown in Fig. 2d. Among three models shown in Fig. 1, the single-layer effective medium model is widely used in various MPA works[1,3,7,25], where the electric and the magnetic resonances lead to the impedance matching condition, $z_{\text{eff}} = \sqrt{\mu_{\text{eff}}/\epsilon_{\text{eff}}} = 1$, at the perfect absorption wavelength. Therefore, the incident EM wave propagates through the top surface of effective film in Fig. 1d without any reflection. Meanwhile, the effective film exhibits large imaginary effective refractive index, $n''_{\text{eff}} \gg n'_{\text{eff}}$, so that the EM wave decays exponentially to zero before it exits from the bottom surface. To verify this interpretation, we use effective medium theory[32] to retrieve the effective permittivity (ϵ_{eff}) and effective permeability (μ_{eff}) from the complex transmission and reflection coefficients, t and r. Due to the asymmetric structure of MPA along the propagation direction of incident light, the perfect absorption only occurs for incident illumination from the front-side (cross-wire) and the EM wave incident from the back-side (MGP) will be totally reflected. Strictly speaking, such extremely asymmetric propagation in MPA cannot be described by waves traveling in a simple medium with homogeneous permittivity and permeability. However, since we only consider the interaction of MPA with incident light from the front-side (cross-wire), we can use t and r for impinging light from the air-side to obtain ϵ_{eff} and μ_{eff} as shown in Fig. 2a,b, respectively. We find a Lorentzian type resonance of ϵ_{eff} at wavelength of 5.13 μm, which can be ascribed to the first-order dipole resonance mode of the cross-wire driven by the electric

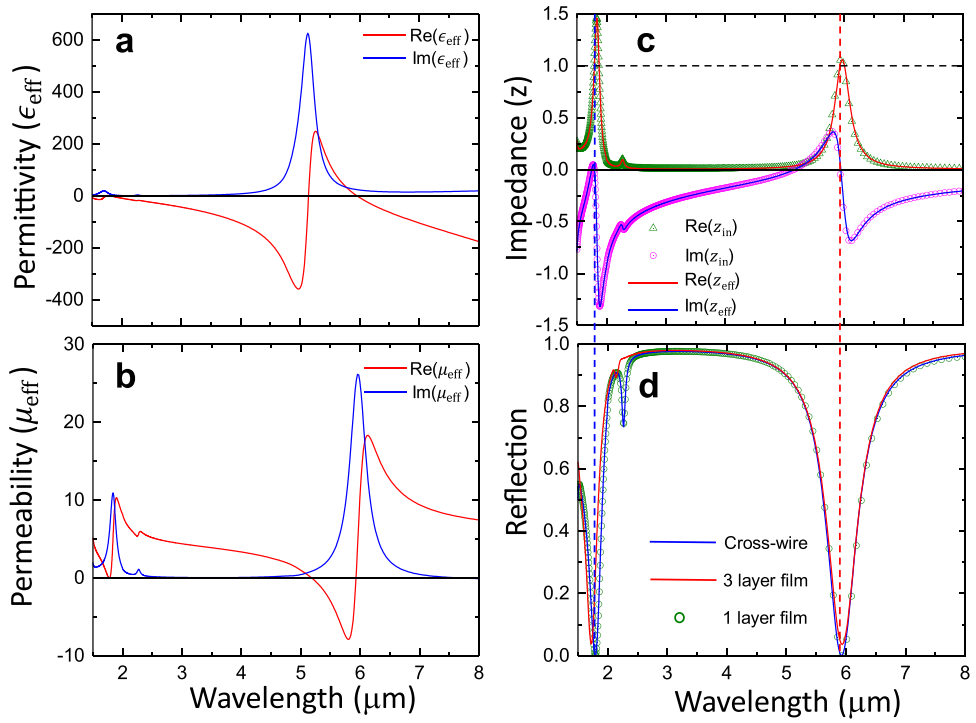

Figure 2. Effective parameters for single-layer effective medium model. Real and imaginary parts of (**a**) effective permittivity and (**b**) effective permeability of MPA retrieved by using a single-layer thin film model. (**c**) Real and imaginary parts effective impedance calculated by single-layer thin film model (z_{eff}, solid curves) and effective circuit model (z_{in}, symbols). (**d**) Simulated reflection spectra of the actual MPA (blue-solid) and structures consisting of single-layer (green-circle) and three-layer (red-sold) effective films.

field of the incident wave. For wavelength $\lambda > 6\ \mu m$, $\mathrm{Re}(\epsilon_{eff})$ is negative. This Drude type response is attributed to the MGP, which exhibits the typical characteristic of permittivity of bulk metal, but with much lower plasma frequency due to diluted average electron density resulting from low volume-ratio of MGP inside the MPA unit cell[33]. The effective permittivity μ_{eff} also shows a Lorentzian type resonance at wavelength of 5.94 μm driven by the magnetic field. This magnetic resonance is induced by the anti-parallel currents on the cross-wire and the MGP, and can be qualitatively explained by the method of image theory[7]. The solid lines in Fig. 2c are the real (red color) and the imaginary (blue color) parts of the effective impedance z_{eff}, which show strong dispersive response as a function of wavelength.

At the perfect absorption wavelength λ = 5.94 μm ($\epsilon_{eff} = 2.432 + 24.175i$ and $\mu_{eff} = 1.003 + 25.517i$), the effective impedance is found to be $z_{eff} = 1.02 + 0.03i$, which matches with the impedance of air ($z_{air} = 1$) very well. The effective refractive index, $n_{eff} = \sqrt{\epsilon_{eff} \cdot \mu_{eff}} = 1.736 + 24.849i$ has a large imaginary part (i.e., $n'' = 24.849$). These calculated effective constitutive parameters very well support the single-layer effective medium model. Specifically, the matched impedance allows the incident wave passing through the top surface of the effective thin film (Fig. 1d) without any reflection. Meanwhile, the intensity of the wave is $I = I_0 e^{-2\alpha z}$, where $\alpha = n'' k = \frac{2\pi n''}{\lambda} = 26.28\,\mu m^{-1}$ (i.e., incident wave decays at a rate of $1/e$ for every 0.019 μm distance traveling inside the MPA). When the incident wave is reflected by MGP and travels a round-trip inside MPA back to the front-surface, its intensity reduces to $I/I_0 = e^{-4\alpha \cdot t_s} = 7.8 \times 10^{-5}$. Thus 99.998% of the wave energy is absorbed inside the MPA. As shown in Fig. 2d, the second absorption peak can be also found at λ = 1.79 μm and the effective impedance $z_{eff} = 1.046 + 0.003i$ is found to be very close to air ($z_{air} = 1$) again. Other effective parameters take the following values: $\epsilon_{eff} = 0.3008 + 7.157i$, $\mu_{eff} = 0.378 + 7.8331i$ and $n_{eff} = 0.338 + 7.49i$. To the best of our knowledge, this second absorption peak (λ = 1.79 μm) has not been thoroughly studied in the past. As will be shown later, it results from the second-order dipole resonance of the cross-wire. The effective impedance of the MPA can also be obtained by the effective circuit model[34]. Figure 1f shows an effective circuit for the MPA, where the MPA is described as a two-port element S in connection with loads z_1 (air) and z_2 (substrate). We calculated the input impedance z_{in} based on transmission line theory and plotted it as triangle (real part) and circle (imaginary part) symbols in Fig. 2c. Although z_{in} was calculated with complete different methodology (see details in Methods section), it shows excellent agreement with z_{eff} obtained from single-layer thin film model. Using the retrieved effective permittivity and permeability $\epsilon_{eff}(\omega)$ and $\mu_{eff}(\omega)$, we performed full-wave simulation for the single-layer effective thin film (Fig. 1d). Figure 2d shows that the simulated reflection (green-circle) completely overlaps the reflection from the original absorber structure (blue-solid line) as expected. The single layer effective medium model can provide fundamental insight for MPA (e.g., reflection and transmission), however this model

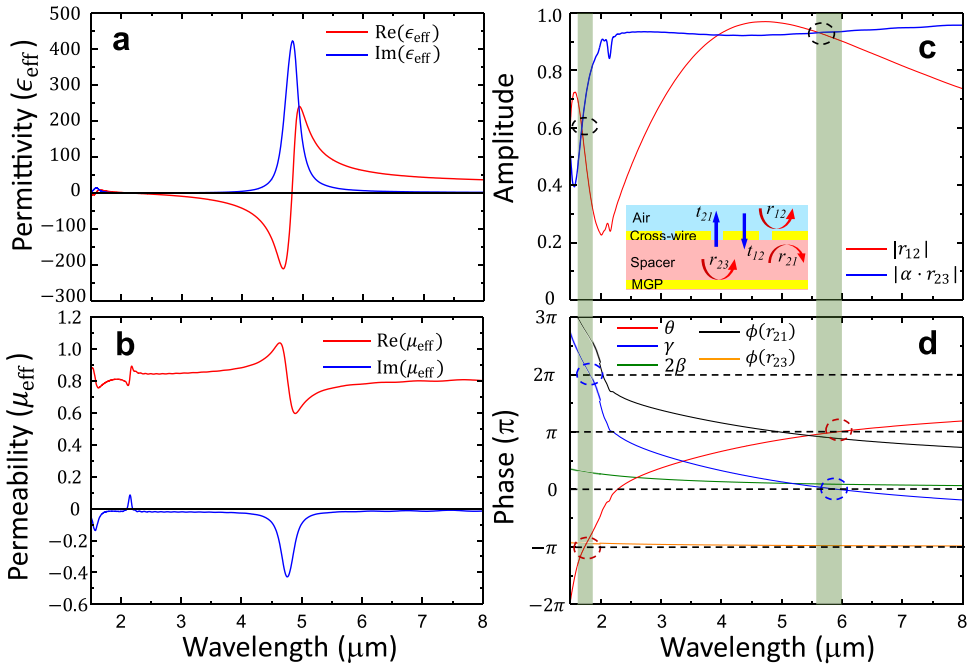

Figure 3. Effective parameters for three-layer effective medium model and perfect absorption conditions. Real (red) and Imaginary (blue) parts of (**a**) effective permittivity (ϵ_{eff}) and (**b**) effective permeability (μ_{eff}). (**c**) $|r_{12}|$ (red) and $|\alpha \cdot r_{23}|$ (blue): terms used in the amplitude condition (Eq. 2). Inset depicts various transmission and reflection coefficients of MPA structure. (**d**) θ (red), γ (blue), 2β (green), $\phi(r_{21})$ (black) and $\phi(r_{23})$ (orange): terms used in the phase condition (Eqs 3, 4). Two perfect absorption regions at 5.94 μm and 1.79 μm are highlighted in green.

cannot provide the microscopic mechanism of the absorption, cannot very well explain NPA and can miss some important features such as ultra-thin thickness.

Three-layer effective medium model. To better understand the underlying mechanism that the wave travels and decays inside the MPA, we have studied the transmission and reflection of waves at each constituting layers and used a transfer matrix method to obtain the overall reflection/absorption properties of MPA. We considered the cross-wire as a metasurface and described it as a homogeneous thin film with effective permittivity ϵ_{eff} and effective permeability μ_{eff}. The effective parameters were calculated using transmission and reflection coefficients of an air/cross-wire/spacer configuration through an improved retrieval method to take account of the asymmetric structure due to different incoming and outgoing medium (air and spacer[35]). As shown in Fig. 3a, the effective permittivity of cross-wire shows a Lorentzian type electric resonance at wavelength of $\lambda_r = 4.75\ \mu m$, which is shorter than the electric resonance obtained by the single-layer model (5.13 μm). The resonance at 4.75 μm is purely electric since the effective permeability (Fig. 3b) takes a constant value of $\mathrm{Re}(\mu_{eff}) = 0.8$ except a typical anti-resonance at λ_r due to the periodicity effect[36]. At wavelength of 1.59 μm, we found the second-order electric dipole resonance mode of the cross-wire, which is much weaker and has negligible influence on the value of ϵ_{eff}. With those values of ϵ_{eff} and μ_{eff}, we used a thin film of the same thickness to replace the cross-wire in the absorber structure. 3D Full-wave simulation of the three-layer thin film model (Fig. 1e) was carried out. The simulated reflection (red-solid curve) is plotted in Fig. 2d, which matches very well with simulation of actual MPA structure (blue-solid) at the first absorption wavelength ($\lambda = 5.94\ \mu m$) and is slightly off at the second absorption wavelength ($\lambda = 1.79\ \mu m$). We ascribe the small discrepancy at $\lambda = 1.79\ \mu m$ to possible effect of MGP on the resonance of cross-wire, which makes slightly noticeable difference of reflections for wavelengths below 2.5 μm. At two absorption peaks, ϵ_{eff} reads value of $64.72 + 7.08i$ and $4.19 + 1.28i$, and μ_{eff} is $0.78 - 0.018i$ and $0.8 - 0.018i$, respectively. The role of the cross-wire can be completely understood as a thin film with these ϵ_{eff} and μ_{eff}. In spite of minor discrepancy at short wavelengths, the excellent agreement between the three-layer thin film model and actual MPA proves that the cross-wire layer and the MGP layer are decoupled, i.e. neither the existence of MGP will affect the resonance of cross-wire nor the resonant current on the cross-wire will affect MGP where the latter only plays a role of a reflecting mirror. Therefore, the transfer matrix method as a common approach to study multiple-layered structure can be used to obtain the overall property of MPA from each layer and to investigate the absorption mechanism of EM waves inside the MPA. The overall reflection of the three-layer structure can be calculated by multiplying the transfer matrix of each layer, $M = M_1 \cdot M_2 \cdot M_3$, as given below (more details can be found in our previous works[27,35]).

$$r = \frac{r_{12} + \alpha r_{23} e^{2i\beta}}{1 - r_{21} r_{23} e^{2i\beta}} \quad (1)$$

In Eq. 1, r_{12} and r_{21} are the reflection coefficients of the cross-wire from front (air)- and back (spacer)-side, respectively. r_{23} is the reflection coefficient of the MGP. $\beta = n_s \cdot k \cdot t_s$ is the propagating phase in the dielectric layer, where n_s, t_s and k are the refractive index, the spacer thickness and the wave vector in free space, respectively. $\alpha = t_{21}t_{12} - r_{21}r_{12}$, where t_{12} and t_{21} are the transmission coefficients through the cross-wire along forward (air/cross-wire/spacer) and backward (spacer/cross-wire/air) directions, respectively. Although α is strictly equal to 1 at the interface between two homogenous media, $\alpha \neq 1$ for the cross-wire around the resonance wavelength. This is caused by the structural asymmetry depending on the propagation direction of incident light. For perfect absorption (i.e., $r = 0$) according to Eq. 1, we obtain the following conditions for the amplitude and the phase, respectively:

$$|r_{12}| = |\alpha \cdot r_{23}| \quad (2)$$

$$\theta = \phi(r_{12}) - \phi(r_{23}) - \phi(\alpha) - 2\beta = (2n + 1)\pi, \quad |n| = 0, 1, 2, \ldots. \quad (3)$$

The coefficients r_{12}, r_{21}, t_{21} and t_{12} are obtained from simulation of the air/cross-wire/spacer configuration and r_{23} is obtained from the simulation of the spacer/MGP configuration.

Around the perfect absorption wavelength $\lambda = 5.94\,\mu m$, both the amplitude condition in Eq. 2 ($|r_{12}| = |\alpha \cdot r_{23}|$) and the phase condition ($\theta = \pi$) are satisfied simultaneously as shown in Fig. 3c and d, respectively. For wavelengths below 5.94 μm, θ decreases as the wavelength decreases and finally reaches $-\pi$ at $\lambda = 1.79\,\mu m$. Meanwhile, the amplitude condition is also satisfied at $\lambda = 1.79\,\mu m$, thereby leading to the second absorption peak. By carefully examining Fig. 3d, we find that the amplitude condition ($|r_{12}| = |\alpha \cdot r_{23}|$ at $\lambda = 5.61\,\mu m$) and the phase condition ($\theta = \pi$ at $\lambda = 5.88\,\mu m$) are not satisfied at exact same wavelength. This explains the fact that the reflection shown in Fig. 2d does not reach zero completely ($\min(|r|^2) = R_{min} = 3.68 \times 10^{-4}$ at $\lambda = 5.94\,\mu m$). The phase condition in Eq. 3 suggests a Fabry-Perot cavity-like mechanism. The cross-wire acts as a "mirror" that reflects light due to its high effective permittivity and forms a cavity together with the MGP. The incident wave enters the MPA and is reflected multiple times by MGP and cross-wire. The FP cavity resonances establish when the round-trip phase is fulfilled with the following condition:

$$\gamma = \phi(r_{21}) + \phi(r_{23}) + 2\beta = 2m\pi, \quad |m| = 0, 1, 2, \ldots. \quad (4)$$

where $\phi(r_{21})$ and $\phi(r_{23})$ are the phases of reflection coefficients at the interfaces of the spacer/cross-wire and the spacer/MGP (Fig. 3d), respectively. When γ equals to $2m\pi$, the waves that travel multiple round-trips between cross-wire and MGP are in phase and hence interfere constructively, thereby leading to resonant cavity modes. As the wavelength decreases, γ (blue curve in Fig. 3d) increases monotonically and reaches the values of 0 and 2π at wavelength of 5.94 μm and 1.82 μm, respectively (matching very well with two perfect absorptions wavelengths). As shown in Fig. 3d, the main contribution to γ comes from $\phi(r_{21})$, which increases from 0.89π to 2.63π as the wavelength decreases from 5.94 μm to 1.82 μm. The significant change of $\phi(r_{21})$ is caused by ϵ_{eff}, which changes from $64.72 + 7.08i$ to $4.19 + 1.28i$ in the same wavelength range as shown in Fig. 3a. Note that the phase condition of Eq. 4 only guarantees the FP cavity modes, resulting in the absorption peaks. To achieve perfect absorption, the amplitude condition in Eq. 2 needs to be satisfied at the same wavelength as well. Nevertheless, Eqs 3 and 4 well explain the NPA peaks of a variety of resonator/spacer/MGP structures that have been widely used in sensing and detecting applications[10–14, 18–21, 28] where the absorption peaks do not necessarily reach 100% (i.e., R = 0). The ultra-thin thickness of MPA can be also explained by the cavity model. As shown in Fig. 3d, at the first perfect absorption wavelength $\lambda = 5.94\,\mu m$ where $\gamma = 0$, the phase $\phi(r_{23}) \approx -\pi$ and $\phi(r_{21})$ is slightly less than π, i.e., $\phi(r_{21}) = \pi - \delta$ with $\delta \ll \pi$. To achieve $\gamma = 0$, it is required $\beta \approx \delta/2$, thus the spacer thickness t_s is found to be $\delta\lambda/4\pi \ll \lambda$. In our simulations, we obtained $\delta = 0.11\pi$ and thus $t_s = 0.0275 \cdot \lambda_s \approx 0.108\ \mu m$, which is close to the actual thickness $t_s = 0.09\ \mu m \approx \lambda_s/44$ where $\lambda_s = \lambda/n_s = 3.94\ \mu m$ being the wavelength inside the spacer medium. This thickness is extremely thin in comparison to a regular FP cavity with size of $\lambda_s/2$. Note that the key fact that leads to this ultra-small size of cavity is $\phi(r_{21})$ being slighly smaller than π due to high effective permittivity of the cross-wire layer.

Another important characteristic feature of MPA is the angular independence of the incident wave. This is very useful in thermal imaging/sensing and energy harvesting applications to receive off-normal incident lights. We performed simulations of actual MPA structure, single-layer and three-layer thin film model with the polar angle θ (in spherical coordinates as displayed in the inset of Fig. 4) of incident wave varying from 0° to 80°. The reflection spectra are shown in Fig. 4a–c for TE wave and Fig. 4a–f for TM wave, respectively. As shown in Fig. 4a, the wavelength of absorption peak at $\lambda = 5.94\,\mu m$ for TE wave does not shift as the incident angle increases from 0° to 80°, showing good angular independence. Reflections of both the single-layer (Fig. 4b) and the three-layer (Fig. 4c) models well match with that of actual MPA structure (Fig. 4a). For TM wave, the reflection of the MPA is blue-shifted as θ is increased by $\Delta_\lambda \equiv \left|\frac{\lambda_{80^\circ} - \lambda_{0^\circ}}{\lambda_{0^\circ}}\right| \sim 4\%$ as shown in Fig. 4d. Both the single-layer and the three-layer models also show the blue-shift with Δ_λ=7.4% and 9.1%, respectively, which is slightly higher than actual MPA. The three-layer model can qualitatively explain the angular dependence for TE and TM modes. The cross-wire layer exhibits an electric resonance excited by the electric field of incident wave. For TE mode, the

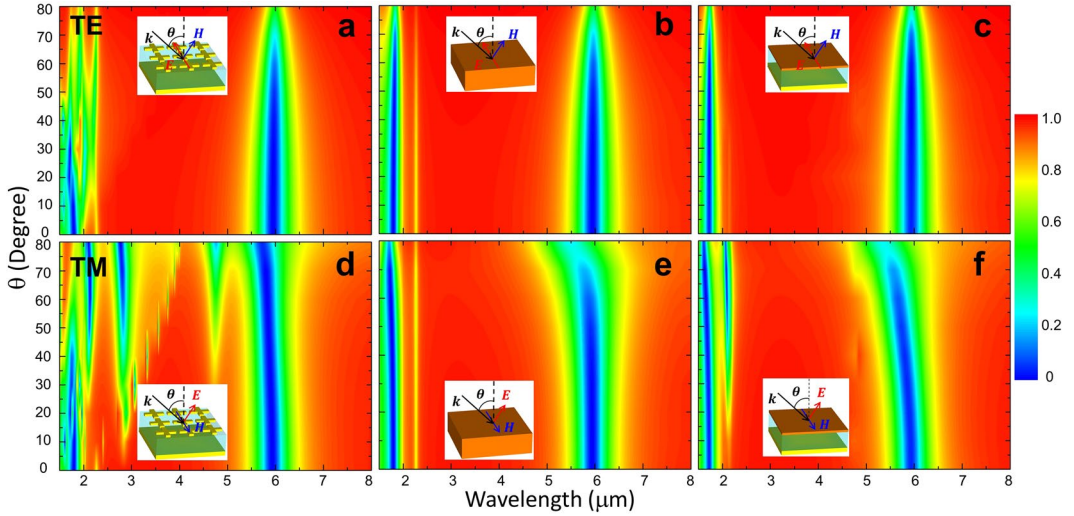

Figure 4. Color plot of angular dependence (θ) of reflection. Reflection for TE-polarized incidence for (**a**) actual MPA structure, (**b**) single-layer thin film model and (**c**) three-layer thin film model. (**d**)–(**f**) Reflection for TM-polarized incidence for corresponding structures.

electric field (See the inset of Fig. 4a) is always parallel to the cross-wire in spite of changing the polar angle θ. Thus, the resonance of cross-wire does not change with incident angle. This leads to the angular independence of absorption for the entire MPA structure. For TM mode, however, the electric field direction changes with θ (see the schematic diagram as shown in the inset of Fig. 4d), resulting in shifting the wavelength of absorption peak. At short wavelengths ($\lambda < p$), incident waves become significantly diffracted through the cross-wires and lead to shifting and splitting of the second absorption peak at λ=1.79 μm as indicated in Fig. 4a and d. These diffractions do not exist for two effective film models as shown in Fig. 4b,c,e and f. In addition, we observed new absorption peaks at around 2.75 μm and 4.75 μm (Fig. 4d) for TM wave, which becomes more significant for $\theta > 50°$. These absorption peaks (reflection dips) result from resonance modes of cross-wires and MGP induced by the vertical component of electric field (E_z), which is nonzero for TM wave and is increased with θ.

Higher order FP modes. Equations 3 and 4 indicate that the phase conditions are satisfied when β increases by an integer multiple of 2π, thereby leading to a series of FP cavity modes. The increment of 2π in β corresponds to an increase in the thickness of spacer (t_s) by $\lambda_s/2$. For the first absorption peak at $\lambda = 5.94$ μm shown in Fig. 2d, the increment of thickness is calculated as $\lambda_s/2 = 1.97\ \mu m$ and the corresponding n-th order thickness is given by $t_{sn} = t_{s1} + n(\lambda_s/2)$ where $t_{s1} = 0.09\ \mu m$ is the thickness of the original MPA. Figure 5a shows the reflection spectra for the three lowest order thickness, $t_{s1} = 0.09\ \mu m$, $t_{s2} = 2.06\ \mu m$ and $t_{s3} = 4.03\ \mu m$. The reflection spectra for the thickness $t_{s2} = 2.06\ \mu m$ (red curve) and $t_{s3} = 4.03\ \mu m$ (blue curve) show the absorption peaks at wavelengths of 5.65 μm and 5.81 μm, respectively, which are well matched with the absorption peak at wavelength of 5.94 μm for the original MPA (i.e., $t_{s1} = 0.09\ \mu m$ for 1st order thickness). We attribute the minor discrepancy in wavelengths to the slight changes of cross-wire resonances due to different separation between cross-wire and MGP. Figure 5b shows the reflections of three-layer thin film model using the same thickness. The results very well match the reflections of actual MPA (Fig. 5a). We recognize these resonances as the three lowest order FP cavity modes, which is confirmed by observing the x-component of electric field E_x inside the MPA structure. The right-side figures in Fig. 5c–e show the real part of E_x along z-direction inside the spacer at the wavelength of absorption peaks, where E_x is evaluated along a straight line in z-direction below the center of cross-wire (from $z = 0$, the bottom of cross-wire to $z = t_{sn}$, the spacer thickness). For the first-order thickness $t_{s1} = 0.09\ \mu m$, $\mathrm{Re}(E_x)$ decreases monotonically from positive value to zero as z increases from 0 (at the cross-wire/spacer interface) to $0.09\ \mu m$ (at the spacer/MGP interface). Such E_x distribution results from the boundary conditions. At the spacer/MGP interface, the high conductivity of MGP forms a "close" boundary where the tangential electric field is forced to be zero ($E_{t,x} = 0$). At the cross-wire/spacer interface, the high effective permittivity ($\epsilon_{\mathrm{eff}} = 64.72 \cdot (1 + 0.11i)$ at λ=5.94 μm) of cross-wire provides a "quasi-open" boundary which allows non-zero tangential electric field ($E_{t,x} \neq 0$). As the thickness of spacer increases to $t_{s2} = 2.06\ \mu m$, a half-period of sine curve is added to E_x field for the first order thickness (E_x as shown on the right side of Fig. 5c) as shown in Fig. 5d, which results in forming the second-order FP cavity mode. Similarly, E_x for $t_{s3} = 4.03\ \mu m$ (Fig. 5e) shows the fundamental mode plus a full-period of sine curve, leading to the third-order FP cavity mode. The three-layer thin film model gives the same E_x profiles as shown in Fig. 5f–h. All the E_x fields for actual MPA (Fig. 5c–e) and for effective thin film model (Fig. 5f–h) exhibit constant phases (not shown here) along z-direction, thereby indicating standing waves as we expected according to the abovementioned FP cavity analysis. The left-side figures in Fig. 5c–e show the electric current distributions on the cross-wire and MGP for the three lowest orders of FP mode. In all three figures, the currents on the cross-wires show a half-wavelength of cosine curve along the

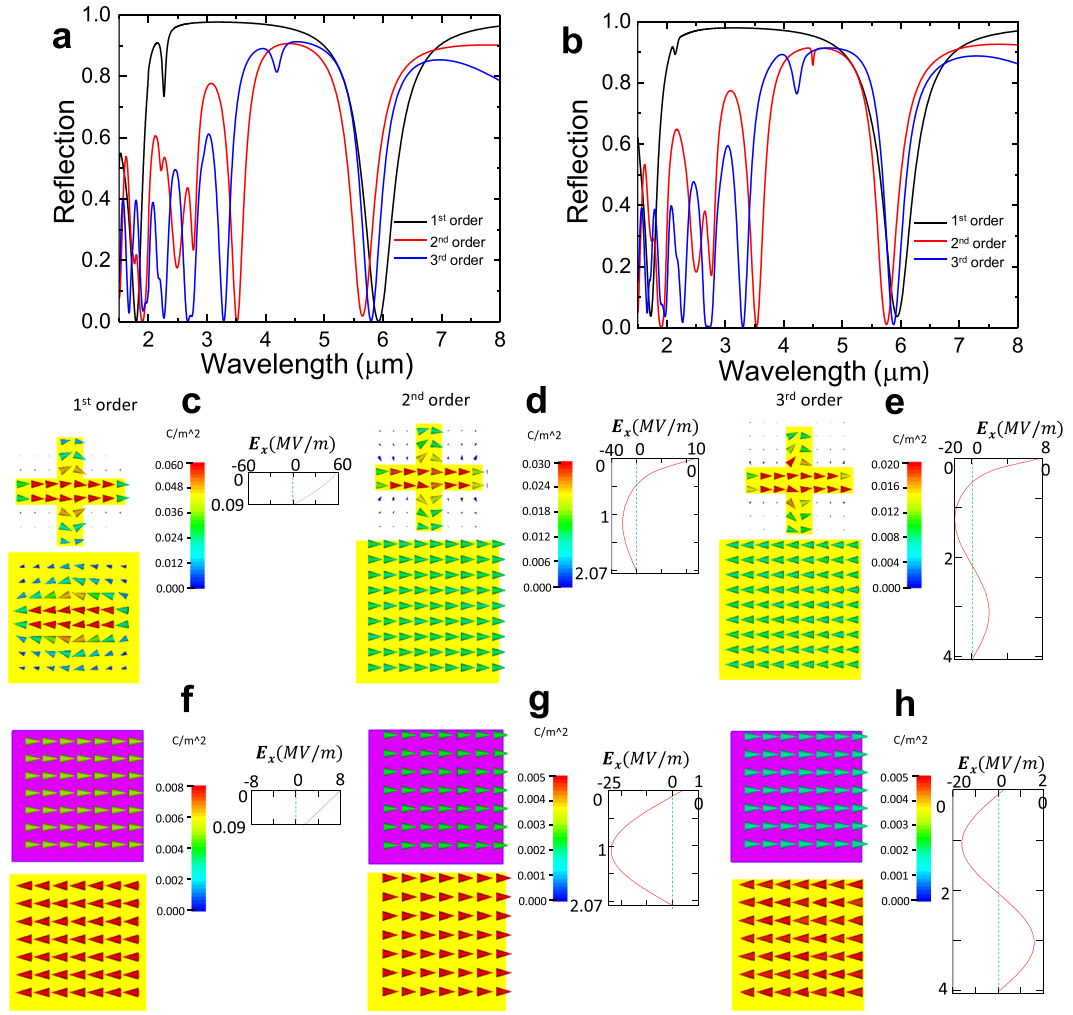

Figure 5. Reflection, E_x field and current distributions for lowest three orders FP modes. (**a**) Simulated reflection spectra for actual MPA structures with the spacer thickness of $t_{s1} = 0.09\ \mu m$ (1st order: black), $t_{s2} = t_{s1} + \lambda_s/2 = 2.06\ \mu m$ (2nd order: red) and $t_{s3} = t_{s1} + \lambda_s = 4.03\ \mu m$ (3rd order: blue). (**b**) The corresponding reflection spectra for three-layer thin film model with spacer thickness $t_{s1} = 0.09\ \mu m$, $t_{s2} = 2.06\ \mu m$ and $t_{s3} = 4.03\ \mu m$. Top views of current density on the cross-wire and MPG for (**c**) 1st order, (**d**) 2nd order and (**e**) 3rd order MPA. Insets placed on the right side of (**c**)–(**e**) show the *x*-component of electric field (E_x) along *z*-direction (propagation direction). Current density on the meta-film representing cross-wire and the MGP for (**f**) 1st order, (**g**) 2nd order and (**h**) 3rd order. Insets on the right side of (**f**)–(**h**) display E_x along *z*-direction for the three-layer thin film structures.

horizontal direction with maximum at the center and zero at ends. This reveals a first-order dipole resonance mode of the cross-wires and matches with the Lorentzian resonance of ε_{eff} shown in Fig. 3a. Figure 5c shows the current on the MGP flowing toward the opposite direction with the maximum current in the center region. The anti-parallel currents on the cross-wire and MGP in Fig. 5c induce a strong magnetic moment that is responsible for the magnetic resonance for single-layer thin film model shown in Fig. 2b. We also observe the same anti-parallel currents in the simulation for the three-layer thin film model as shown in Fig. 5f. Such current distributions can be well explained by the E_x profile shown in Fig. 5f. The tangential electric field $E_{t,x}$ induces the electric current, $J_x = i\omega\epsilon E_{t,x}$, where the ϵ for cross-wire and MGP are given by ϵ_{eff} and ϵ_{MGP} (using the Drude model[31]) respectively. At wavelength of $\lambda = 5.94\,\mu\text{m}$, the real parts of ϵ for cross-wire and MGP have the opposite signs, i.e., $\text{Re}(\epsilon_{eff}) > 0$ and $\text{Re}(\epsilon_{\text{MGP}}) < 0$. For the first-order cavity shown in Fig. 5c,f, E_x in metafilm and MGP are in phase, and thereby result in anti-parallel currents. For the higher order cavities (e.g. Figure 5g,h for the second- and third-order cavities, respectively), when t_s is increased by $\lambda_s/2$, the phase of E_x in MGP increases by π and the current in MPG changes to the opposite direction.

We expect the FP cavity model for MPA to lead to novel applications. As one example, the MPA provides much stronger local electromagnetic fields enhancement than typical plasmonic resonators due to its large Q-factor. Such local field enhancement is always demanded to improve the performance of sensor/detector at infrared and THz regimes[11,21,37]. However, the region between resonator and MGP in the MPA, where the fields are mostly enhanced, are too thin to fit most sensing and detector devices. With the cavity model, we can design

the higher order cavities that can fit in the required thickness of practical devices. For instance, infrared focal plane array device working at 6 μm wavelength[37], is composed of an active layer (20 stacks of InGaAs/AlGaAs quantum wells) and top/bottom contact layers (n-doped GaAs). The total thickness is about 2 μm which is much larger than the first-order MPA thickness of 0.09 μm, but is very close to the second-order thickness of 2.06 μm. Furthermore, this thickness is tunable by varying the size of the resonator (cross-wire) to fit the requirement of existing devices. Another potential application is to use the high photonic density of states (PDOS) for cavity quantum electrodynamic (QED) applications[29,38,39]. PDOS is inversely proportional to the volume of a cavity. The first-order cavity of MPA has thickness of ~$\lambda/44$, much smaller than typical FP cavity ($\lambda/2$). This size is also much smaller than typical plasmonic resonators[29] which EM fields normally extend to distance of a few wavelengths. Our calculation shows the MPA cavity can improve the PDOS by ~80 times as compared to plasmonic resonators. Such high PDOS promises great potential in cavity QED applications[29,38,39].

Discussion

In summary, we developed a multi-layered metasurface model for MPA. With a transfer matrix analysis, we found a FP cavity mechanism that models the MPA as a meta-cavity bounded between the "qusi-open" boundary of resonator and the "close" boundary of MGP. The FP cavity model well explains the characteristic features including ultra-thin thickness and angular independence. We also found the higher order FP cavity modes when the thickness of MPA (spacer) increases by multiples of a half-wavelength. The strong field enhancement of cavity resonances and high PDOS promise novel applications in sensor/detector and cavity QED device.

Methods

The effective impedance z_{in} of the circuit model is calculated from the reflection coefficients Γ_{in} and Γ_{out} at the the input and output termial of S, using the following equations[34]:

$$\Gamma_{in} = S_{11} + \frac{S_{12}\Gamma_{out}S_{21}}{1 - r_2 S_{22}} \tag{5}$$

$$\Gamma_{out} = S_{22} + \frac{S_{12}\Gamma_{in}S_{21}}{1 - r_1 S_{11}} \tag{6}$$

where S_{11}, S_{12}, S_{21} and S_{22} are the S-parameters, which can be obtained from simulations of entire MPA structure. The coupled equations (Eqs 5 and 6) can be solved analytically:

$$\begin{aligned}\Gamma_{in} = & -\frac{1}{2(s_{11} + s_{12}s_{21}s_{22} - s_{11}s_{22}^2)}(s_{12}^2 s_{21}^2 - 2s_{11}s_{12}s_{21}s_{22} + (1 + s_{11}^2)(-1 + s_{22}^2) \\ & + \sqrt{-4(s_{11}s_{12}s_{21} + s_{22} - s_{11}^2 s_{22})^2 + (1 - s_{12}^2 s_{21}^2 + 2s_{11}s_{12}s_{21}s_{22} + s_{22}^2 - s_{11}^2(1 + s_{22}^2)^2)^2})\end{aligned} \tag{7}$$

$$\begin{aligned}\Gamma_{out} = & \frac{1}{(-2s_{11}s_{12}s_{21} + 2(-1 + s_{11}^2)s_{22})}(s_{12}^2 s_{21}^2 - 2s_{11}s_{12}s_{21}s_{22} + (-1 + s_{11}^2)(1 + s_{22}^2) + \\ & \sqrt{-4(s_{11}s_{12}s_{21} + s_{22} - s_{11}^2 s_{22})^2 + (1 - s_{12}^2 s_{21}^2 + 2s_{11}s_{12}s_{21}s_{22} + s_{22}^2 - s_{11}^2(1 + s_{22}^2)^2)^2})\end{aligned} \tag{8}$$

We then solved the input and output impedances from Γ_{in} and Γ_{out}:

$$z_{in} = \frac{1 + \Gamma_{in}}{1 - \Gamma_{in}} \tag{9}$$

$$z_{out} = \frac{1 + \Gamma_{out}}{1 - \Gamma_{out}} \tag{10}$$

For MPA, we only consider the input impedance z_{in} as shown in Fig. 1f for the incident wave from the front side.

References

1. Watts, C. M., Liu, X. L. & Padilla, W. J. Metamaterial Electromagnetic Wave Absorbers. *Advanced Materials* **24**, 98–120 (2012).
2. Hedayati, M., Faupel, F. & Elbahri, M. Review of Plasmonic Nanocomposite Metamaterial Absorber. *Materials* **7**, 1221–1248 (2014).
3. Landy, N. I., Sajuyigbe, S., Mock, J. J., Smith, D. R. & Padilla, W. J. Perfect metamaterial absorber. *Physical Review Letters* **100**, 207402 (2008).
4. Seren, H. R. *et al.* Optically Modulated Multiband Terahertz Perfect Absorber. *Advanced Optical Materials* **2**, 1221–1226 (2014).
5. Shrekenhamer, D., Montoya, J., Krishna, S. & Padilla, W. J. Four-Color Metamaterial Absorber THz Spatial Light Modulator. *Advanced Optical Materials* **1**, 905–909 (2013).
6. Savo, S., Shrekenhamer, D. & Padilla, W. J. Liquid Crystal Metamaterial Absorber Spatial Light Modulator for THz Applications. *Advanced Optical Materials* **2**, 275–279 (2014).
7. Tao, H. *et al.* A metamaterial absorber for the terahertz regime: Design, fabrication and characterization. *Optics Express* **16**, 7181–7188 (2008).
8. Hao, J. M. *et al.* High performance optical absorber based on a plasmonic metamaterial. *Applied Physics Letters* **96**, 251104 (2010).
9. Liu, X. *et al.* Taming the Blackbody with Infrared Metamaterials as Selective Thermal Emitters. *Physical Review Letters* **107**, 045901 (2011).
10. Maier, T. & Brückl, H. Wavelength-tunable microbolometers with metamaterial absorbers. *Optics Letters* **34**, 3012–3014 (2009).

11. Jing, Y. L. *et al*. Pixel-level plasmonic microcavity infrared photodetector. *Sci Rep* **6**, 25849 (2016).
12. Zhang, C., Chang, H. T., Zhao, F. Y. & Hu, X. H. Design principle of Au grating couplers for quantum-well infrared photodetectors. *Optics Letters* **38**, 4037–4039 (2013).
13. Chang, H., Zhang, C., Zhao, F. & Hu, X. Antireflection Coatings on Au Plasmonic Gratings for Infrared Photodetection. *Plasmonics* **10**, 1519–1524 (2015).
14. Zhao, F., Zhang, C., Chang, H. & Hu, X. Design of Plasmonic Perfect Absorbers for Quantum-well Infrared Photodetection. *Plasmonics* **9**, 1397–1400 (2014).
15. Wang, Z. *et al*. Circular Dichroism Metamirrors with Near-Perfect Extinction. *ACS Photonics* **3**, 2096–2101 (2016).
16. Li, W. *et al*. Circularly polarized light detection with hot electrons in chiral plasmonic metamaterials. *Nat Commun* **6**, 8379 (2015).
17. Plum, E. & Zheludev, N. I. Chiral mirrors. *Applied Physics Letters* **106**, 221901 (2015).
18. Tittl, A. *et al*. Palladium-Based Plasmonic Perfect Absorber in the Visible Wavelength Range and Its Application to Hydrogen Sensing. *Nano Letters* **11**, 4366–4369 (2011).
19. Liu, N., Mesch, M., Weiss, T., Hentschel, M. & Giessen, H. Infrared Perfect Absorber and Its Application As Plasmonic Sensor. *Nano Letters* **10**, 2342–2348 (2010).
20. Li, G. H. *et al*. A novel plasmonic resonance sensor based on an infrared perfect absorber. *J Phys D Appl Phys* **45**, 205102 (2012).
21. Bhattarai, K. *et al*. A Large-Area, Mushroom-Capped Plasmonic Perfect Absorber: Refractive Index Sensing and Fabry-Perot Cavity Mechanism. *Advanced Optical Materials* **3**, 1779–1786 (2015).
22. Liu, X., Starr, T., Starr, A. F. & Padilla, W. J. Infrared spatial and frequency selective metamaterial with near-unity absorbance. *Phys Rev Lett* **104**, 207403 (2010).
23. Hedayati, M. K. *et al*. Design of a Perfect Black Absorber at Visible Frequencies Using Plasmonic Metamaterials. *Advanced Materials* **23**, 5410 (2011).
24. Wang, B. N., Koschny, T. & Soukoulis, C. M. Wide-angle and polarization-independent chiral metamaterial absorber. *Physical Review B* **80**, 033108 (2009).
25. Tittl, A. *et al*. Quantitative Angle-Resolved Small-Spot Reflectance Measurements on Plasmonic Perfect Absorbers: Impedance Matching and Disorder Effects. *Acs Nano* **8**, 10885–10892 (2014).
26. Chen, H.-T. Interference theory of metamaterial perfect absorbers. *Optics Express* **20**, 7165–7172 (2012).
27. Zhou, J. *et al*. Application of metasurface description for multilayered metamaterials and an alternative theory for metamaterial perfect absorber. *arXiv:1111 0343v1* (2011).
28. Shen, Y. *et al*. Plasmonic gold mushroom arrays with refractive index sensing figures of merit approaching the theoretical limit. *Nat Commun* **4**, 2381 (2013).
29. Tanaka, K., Plum, E., Ou, J. Y., Uchino, T. & Zheludev, N. I. Multifold enhancement of quantum dot luminescence in plasmonic metamaterials. *Phys Rev Lett* **105**, 227403 (2010).
30. CST Micwave Studio: A numerical simualtion software for electromagnetic computing, Computer Simulation Technology GmbH, Darmstadt, Germany. https://www.cst.com/.
31. Ordal, M. A., Bell, R. J., Alexander, R. W. Jr., Long, L. L. & Querry, M. R. Optical properties of fourteen metals in the infrared and far infrared: Al, Co, Cu, Au, Fe, Pb, Mo, Ni, Pd, Pt, Ag, Ti, V, and W. *Applied optics* **24**, 4493 (1985).
32. Smith, D. R., Schultz, S., Markos, P. & Soukoulis, C. M. Determination of effective permittivity and permeability of metamaterials from reflection and transmission coefficients. *Physical Review B* **65**, 195104 (2002).
33. Pendry, J. B., Holden, A. J., Stewart, W. J. & Youngs, I. I. Extremely low frequency plasmons in metallic mesostructures. *Phys Rev Lett* **76**, 4773–4776 (1996).
34. Mazilu, M. & Dholakia, K. Optical impedance of metallic nano-structures. *Optics Express* **14**, 7709–7722 (2006).
35. Jeon, J. *et al*. A Low-loss Metasurface Antireflection Coating on Dispersive Surface Plasmon Structure. *Sci Rep* **6**, 36190 (2016).
36. Koschny, T., Markos, P., Smith, D. R. & Soukoulis, C. M. Resonant and antiresonant frequency dependence of the effective parameters of metamaterials. *Physical review E, Statistical, nonlinear, and soft matter physics* **68**, 065602 (2003).
37. Lee, S. J. *et al*. A monolithically integrated plasmonic infrared quantum dot camera. *Nat Commun* **2**, 286 (2011).
38. Sato, Y. *et al*. Strong coupling between distant photonic nanocavities and its dynamic control. *Nat Photon* **6**, 56–61 (2012).
39. Scalari, G. *et al*. Ultrastrong Coupling of the Cyclotron Transition of a 2D Electron Gas to a THz Metamaterial. *Science* **335**, 1323–1326 (2012).

Acknowledgements

The USF portion of this work was supported by the Alfred P. Sloan Research Fellow grant FG-BR2013-123 and by KRISS grant GP2016-034. The KRISS portion of this work was supported by the KRISS grant GP2016-034 and the AOARD grant FA2386-14-1-4094 funded by the U.S. government (AFOSR/AOARD). The NWPU portion of this work was supported by the National Natural Science Foundation of China (Grant No. 61601375) and the Fundamental Research Funds for the Central Universities (Grant No. 3102016ZY029).

Author Contributions

K.B. and J.Z. performed numerical simulations. K.B., S.S., S.K., Z.K. and J.Z. developed the multiple layer model and retrieval method, and performed analytical analysis of the MPA mechanism. J.Z., Z.K. and K.B. wrote the manuscript. S.J.L., A.U., Z.K. and J.Z. supervised the work.

Additional Information

Competing Interests: The authors declare that they have no competing interests.

Publisher's note: Springer Nature remains neutral with regard to jurisdictional claims in published maps and institutional affiliations.

Open Access This article is licensed under a Creative Commons Attribution 4.0 International License, which permits use, sharing, adaptation, distribution and reproduction in any medium or format, as long as you give appropriate credit to the original author(s) and the source, provide a link to the Creative Commons license, and indicate if changes were made. The images or other third party material in this article are included in the article's Creative Commons license, unless indicated otherwise in a credit line to the material. If material is not included in the article's Creative Commons license and your intended use is not permitted by statutory regulation or exceeds the permitted use, you will need to obtain permission directly from the copyright holder. To view a copy of this license, visit http://creativecommons.org/licenses/by/4.0/.

© The Author(s) 2017